J. Fluid Mech. (1988), *vol.* 189, *pp.* 87–116
Printed in Great Britain

Three-dimensional shear layers via vortex dynamics

By W. T. ASHURST
Sandia National Laboratories, Livermore, CA 94550, USA

AND ECKART MEIBURG
Division of Applied Mathematics, Brown University, Providence, RI 02912, USA

(Received 14 November 1986 and in revised form 16 July 1987)

The evolution of the two- and three-dimensional structures in a temporally growing plane shear layer is numerically simulated with the discrete vortex dynamics method. We include two signs of vorticity and thus account for the effect of the weaker boundary layer leaving the splitter plate which is used to create a spatially developing mixing layer. The interaction between the two layers changes the symmetry properties seen in a single vorticity-layer calculation and results in closer agreement with experimental observations of the interface between the two streams. Our calculations show the formation of concentrated streamwise vortices in the braid region between the spanwise rollers, whereas the spanwise core instability is observed to grow only initially. Comparison with flow visualization experiments is given, and we find that the processes dominating the early stages of the mixing-layer development can be understood in terms of essentially inviscid vortex dynamics.

1. Introduction

The motivation for studying the two- and three-dimensional instability mechanisms of the plane mixing layer is twofold: this flow represents one of the well-defined base flows for the investigation of generic formation processes that lead to complex three-dimensional structures, and at the same time it also approximates situations of considerable practical interest such as the flows in a chemical reactor, in a combustion chamber, and behind an airfoil. The work of Brown & Roshko (1974) revealed the existence of coherent two-dimensional vortical structures in a high-Reynolds-number turbulent planar mixing layer. Discrete vortex dynamics simulations (Ashurst 1979) have reproduced the generation of these structures as well as the pairing process, which represents the primary growth mechanism of the layer, and the related turbulent shear stress. Further experimental investigations (Konrad 1976; Bernal 1981; Breidenthal 1981; Jimenez 1983) indicate that there is a secondary vortex structure in the flow direction. This streamwise vorticity apparently arises from natural instability to three-dimensional perturbations. Clean, laminar initial conditions can postpone its appearance until four or five wavelengths of the Kelvin–Helmholtz instability downstream of the splitter plate. However, deliberate localized or periodic disturbances create streamwise structures which are similar in their behaviour to the naturally turbulent flow (Lasheras, Cho & Maxworthy 1986; Lasheras & Choi 1988). As long as the outer boundary conditions maintain the velocity difference across the layer, the Kelvin–Helmholtz instability continues to generate the two-dimensional spanwise vorticity structure, while the secondary structure appears to 'lock in' to a spanwise spacing and location which it

can maintain even through several pairings of the two-dimensional structure. It is still not clear exactly how the streamwise vorticity is formed. Bernal infers from his experiments the presence of vortex lines alternatingly wrapping around the upstream and the downstream roller, thus resulting in pairs of counter-rotating streamwise vortices in the thin vorticity region (the braids) between the spanwise vortices. Breidenthal, on the other hand, observes an undulation of the core of the spanwise vortices which then develops into streamwise vorticity in the strain field of the neighbouring rollers. While the observations of Breidenthal and Bernal demonstrate the presence of streamwise vorticity both in the core and in the braid regions, they do not resolve the question of where it originates.

The evolution of three-dimensional disturbances in a plane shear layer has also been investigated by means of linear stability calculations. Pierrehumbert & Widnall (1982) theoretically analyse a periodic array of Stuart vortices and show the existence of an instability mode of the vortex cores. They conclude that the wiggle of the cores of the spanwise vortices observed by Breidenthal might be a manifestation of this instability. Corcos & Lin (1984) criticize this work of Pierrehumbert & Widnall on the grounds that the background vorticity pattern selected has a symmetry that is not produced by the Kelvin–Helmholtz instability. Consequently, Corcos & Lin try an alternative approach of solving a two-dimensional problem coupled to the spanwise average of a three-dimensional velocity field. They conclude that in the presence of the two-dimensional pairing instability, there will be only slight effects from three-dimensional instabilities on the overall growth of the layer, but their work does not deal with the identification of a most amplified spanwise wavelength. Lin & Corcos (1984) assume that if the spanwise vorticity is deformed, then there will be regions of alternating signs of streamwise vorticity which are subjected to a streamwise strain. They numerically integrate this model problem and find that sheets of streamwise vorticity may collapse to concentrated round vortex filaments under certain conditions of strain, spacing and viscosity values. Neu (1984) presents an analytical theory of this phenomenon. As a result, while not knowing the details of the formation process, it can be concluded that alternating regions of streamwise vorticity may, in the strain field of the two-dimensional structures, form very concentrated vortex filaments in the streamwise direction, which do not inhibit further two-dimensional pairing.

Two recent calculations may indicate the generic formation process of streamwise vorticity. In a model problem calculation, Aref & Flinchem (1984) consider the dynamics of a vortex filament when the Biot-Savart interaction is truncated to the velocity that is induced by the local filament curvature. In this approximation, soliton waves may propagate along the filament. They calculate the response of such a wave when a mean shear velocity is added: the wave now no longer behaves like a soliton and instead produces spanwise wiggles with a wavelength that depends on the filament circulation and the applied shear rate. Pierrehumbert (1986) arrives at the same result by analysing the linear instability characteristics of the local induction approximation. A more complete calculation by Rogers & Moin (1987) substantiates this physical picture. By means of a direct simulation based on the Navier–Stokes equations on a 128^3 grid they investigate the evolution of small random fluctuations of the flow variables under the influence of a mean shear. It is observed that the vorticity fluctuations are stretched out in the direction of the major strain axis and in this process become more concentrated, thus leading to a preponderance of horseshoe vorticity. The legs of these horseshoes disappear into the background random vorticity field. These observations suggest that some knowledge

about the formation process of the streamwise structures can be gained from an analysis of inviscid vorticity dynamics. Consequently, it is appealing to simulate the mixing layer by means of a three-dimensional vortex filament calculation with the full Biot-Savart interaction.

Three-dimensional vortex dynamics simulations are possible on today's computers (Leonard 1985). Lagrangian tracking of the filaments replaces difficulties associated with numerical diffusion in finite difference solutions of the Navier–Stokes equations. Since only the vorticity field must be discretized instead of the complete velocity field, there is also the economy of an adaptive mesh. A discouraging feature is the ever increasing growth rate of the filament arclength in three-dimensional inviscid flows (Siggia 1985). Vortex stretching renders the calculations very costly or requires a very small computational domain. Even with these limitations, the numerical integration of this dynamical problem presents a promising way to gain insight into the evolution of a shear layer, since this approach allows us to specify precisely initial perturbations in a nominally two-dimensional flow and then track their growth well into the nonlinear regime.

In contrast to our Lagrangian calculation, Riley, Metcalfe & Orszag (1986) have done a direct Navier–Stokes simulation of a three-dimensional shear layer on a 64^3 mesh in which one streamwise wavelength was tracked. They consider small random disturbances in all velocity components in addition to a hyperbolic tangent profile of the velocity in the flow direction. The maximum Reynolds number based on the Taylor microscale is 50, which is much lower than the corresponding values in many experiments and indicates that small-scale effects will be suppressed by viscous diffusion. The developing small scales, e.g. the thinning of the braid region and the evolution of streamwise streaks or horseshoe vortices, present a difficulty for the direct method which sets a viscosity and resolves all lengthscales. These developing small scales either require a large number of grid points (especially since to achieve computational speed these direct methods use fast Fourier transforms which require a uniform mesh spacing and thus cannot adapt a local region except by coordinate transformations) or a large viscosity value and hence a low Reynolds number. As we will discuss later, the vortex method also has limitations, and the two methods should be used to complement each other.

The outline of this paper is as follows: in §2 we give the details of our computational technique, and in §3 the simulation results are presented. We first discuss, in §3.1, the simpler case in which a shear layer is represented by one sign of vorticity. At the suggestion of Paul Dimotakis we also investigated the more complicated case which includes two signs of vorticity. Measurements by Lang (1985) and Dimotakis of spanwise vorticity (laser measured velocity at four points) indicates that the weaker boundary-layer vorticity is observed at downstream locations and becomes distributed across the mixing layer. This observation points towards a mingling of the two signs of vorticity without local cancellation and with the possibility that imperfect filaments of the weaker layer in the strain field formed by the Kelvin–Helmholtz instability might lead to the formation of streamwise vorticity. These simulations are presented in §3.2. Motivated by the experimental investigation of Lasheras *et al.* (1986), we attempted to analyse the effect of a strong localized perturbation, which is discussed in §3.3. In §4 we compare our numerical results with experimental observations, emphasizing the progressive deformation and growth of the interface between the two boundary layers leaving the splitter plate. Concluding remarks are given in §5.

2. The vortex dynamics method

Our goal is to simulate numerically an unbounded incompressible flow field of which only a small portion is rotational. Thus, it is convenient to formulate the problem in terms of the vorticity variable. Its definition along with the condition of non-divergent velocity allows a complete description of the flow kinematics from the Biot-Savart law (e.g. Batchelor 1967). For this purpose, we discretize the vorticity field into continuous filaments, which are represented by a number of node points along their centrelines. The node velocities are evaluated according to a modified Biot-Savart law and the temporal evolution of the flow can then be obtained by advancing the nodes over a small timestep with their respective velocities. The modification to the Biot-Savart law is the assumption of an invariant vorticity distribution around the filament, based on the functional form

$$\gamma(\boldsymbol{x}-\boldsymbol{r}) = \frac{3\alpha\sigma^2}{4\pi(|\boldsymbol{x}-\boldsymbol{r}|^2+\alpha\sigma^2)^{\frac{5}{2}}}, \tag{1}$$

where we use the notation of Leonard (1985). This assumption is advantageous in that a node velocity may be found by one integration along the filament arclength and that no velocity singularities will be generated. However, the assumption is detrimental in that no changes in the vorticity shape will occur due to a small-scale strain effects and thus, it determines a small-scale resolution limit. The vorticity distribution from a filament with circulation Γ follows as

$$\omega(\boldsymbol{x},t) = \Gamma\int_C \gamma[\boldsymbol{x}-\boldsymbol{r}(s)]\frac{\partial \boldsymbol{r}(s)}{\partial s}\,\mathrm{d}s, \tag{2}$$

where $\boldsymbol{r}(s)$ describes the filament centreline in terms of the arclength s. Here the combination of $\alpha\sigma^2$ is a measure of the vortical domain. Following earlier studies (cf. Leonard 1985, p. 528) which considered constant vorticity within a tube and zero vorticity outside the tube, we will refer to σ as the core radius and adjust the value of α to reflect other possible distributions of vorticity. If a vortex ring with a Gaussian vorticity distribution is simulated by a single vortex filament with the above vorticity distribution, then the self-induced velocity is correctly reproduced when α has the numerical value of 0.413. As a result, we have used this value exclusively throughout our simulations, and we will use 2σ as the reference length, see below.

The vorticity of an infinitely long straight filament with the smoothing of equation (1) decays like the inverse fourth power of the distance from the filament. The two-dimensional stream function related to this infinite filament behaves like $\ln(|\boldsymbol{x}-\boldsymbol{r}|^2+\alpha\sigma^2)$, and its velocity profile is similar to the exponential profile obtained as the time-dependent solution for the viscous diffusion of the vorticity from an isolated line source.

Incorporation of this vorticity distribution into the Biot-Savart law then allows us to obtain the velocity $\boldsymbol{u}$ at any position x by integrating over the arc length of all N filaments in the flowfield

$$\boldsymbol{u}(\boldsymbol{x},t) = -\frac{1}{4\pi}\sum_{i=1}^{N}\Gamma_i\int_{C_i}\frac{[\boldsymbol{x}-\boldsymbol{r}_i(s,t)]\times\hat{\boldsymbol{t}}(s)}{([\boldsymbol{x}-\boldsymbol{r}_i(s,t)]^2+\alpha\sigma_i^2)^{\frac{3}{2}}}\mathrm{d}s \tag{3}$$

where $\hat{\boldsymbol{t}}(s)$ is the filament tangent vector. This modified Biot-Savart law has a velocity that remains bounded even for $\boldsymbol{x}-\boldsymbol{r}(s)\to 0$. When using this equation to

evaluate the influence of filament i on filament j we replace σ_i^2 by $\frac{1}{2}(\sigma_i^2+\sigma_j^2)$ to conserve linear and angular momentum, as proposed by Leonard (1980). The filament radius σ_i is kept uniform along the arclength but changes with time to maintain a constant filament volume. This procedure conserves energy if the cores do not overlap. A more costly scheme suggested by Leonard (1980) conserves energy even if the cores do overlap by determining an average velocity over the cross-section of the filament (the smoothing distribution is the weighting function and the σ_i are now constant in time). While vorticity volume is not conserved, it is no longer appropriate to think of these filaments as isolated vortex tubes. To our knowledge, this scheme has yet to be tried. Overlap of the filament cores, however, provides a smoother distribution of the vorticity and, as described below, has been shown to be necessary for convergence to the Euler equations.

There has been new work on convergence proofs of vortex schemes, and §4 of Anderson & Greengard (1985) gives a description of two possible choices in three-dimensional vortex modelling: (i) connected filaments where the vortex stretching is naturally found by the change in filament length and (ii) disconnected discrete vortices where local strain must be calculated in order to change the vorticity magnitude. Beale (1986) gives a convergence proof of the second scheme and Greengard (1986) a proof of the connected filament method, but his proof does not consider the addition of node points in order to resolve large strain effects. The style of these proofs is to bound the errors in the discrete velocity versus the exact velocity from a known vorticity distribution. A sufficiently smooth initial distribution is assumed, the smoothness determines the time interval in which the error estimates are valid. Stability is shown in the sense that sufficiently small errors in the computed motion yield bounded errors in velocity. These proofs indicate that the vortex core term should be larger than the inter-vortex spacing as both parameters are reduced to zero. Conservation of energy is not discussed, the difficulty being that with finite cores there is no closed-form expression for the energy density. If we modify the energy integral in the same manner as was done to the Biot-Savart integral, then we add the core term to the inverse distance factor in the integrand of scalar products of the vorticity vectors (see Lamb 1932, p. 217). The resulting energy quantity is not constant when multiple filaments interact at distances which are not large with respect to the core size. However, in cases where the filaments do have large separation before and after a close encounter, we do find this modified energy term returning to its initial value. For example, consider two ring vortices moving in the same direction with a common axis, each ring described as one filament. In this symmetric configuration, the rings will alternate in passing through each other, the smoke-ring problem. The modified energy integral value will oscillate about a mean value, the amplitude of the oscillation depending on the variation in the closest approach to the largest separation. The mean value decreases with time but the decay rate is dependent on the selected integration scheme and error tolerances.

Considering that the convergence proofs are still limited in their applications, then simulations of known problems can be used to calibrate a numerical scheme. In two dimensions an obvious case is the inviscid Kelvin–Helmholtz instability of a shear layer. In order to reproduce closely the desired velocity profile, Nakamura, Leonard & Spalart (1982) used many layers of discrete vortices and examined the core-size effect in terms of the inter-vortex spacing. As we stated before, they find core overlap is desirable. However, because we wish to simulate three-dimensional shear layers and need as few vortices as possible, we studied the same two-dimensional problem but with only one layer of discrete vortices. The growth rates of long wavelength

disturbances have the correct trend, but we obtain growth rates which are too large for short wavelengths. In these calculations a symmetric core distribution of vorticity with constant size is maintained when, in fact, the strain field should be able to distort the vorticity distribution about each discrete vortex; this may explain the discrepancy observed for small wavelengths. Thus, we will use long-wavelength disturbances in this work.

In three dimensions, Kelvin's analysis of bending modes for a rectilinear vortex tube provides another calibration problem for the vortex method. It should be kept in mind, however, that the following results were obtained for an isolated filament and might not hold for a collection of overlapping filaments. When compared to Kelvin's calculation for a single filament with uniform vorticity within a core of radius σ, the correct long-wavelength limit instability ($\kappa\sigma \to 0$, where κ is the wavenumber) is obtained with the modified Biot-Savart integral, but in addition, a spurious short-wave instability is observed for $\kappa\sigma$ near 2.3 (see figure 3 in Leonard 1985). This instability is close in its wavelength to a physical higher radial mode instability at $\kappa\sigma = 2.5$ for which the circular cross-section becomes elliptical (Tsai & Widnall 1976; Robinson & Saffman 1984), but we have no reason to assume dynamical similarity. Thus, the modified Biot-Savart relation yields instabilities at both long and short wavelengths. As we will see, the short-wave instability creates numerical difficulties by producing high filament curvature and thus requiring many node points along the filament. In summary, we have a scheme which conserves linear and angular momentum without generating velocity singularities, but which does not strictly conserve energy and may not have the proper instability growth rate in the short-wavelength limit but does capture the long-wavelength instability; therefore, for the most part, we restrict the initial perturbations to long wavelengths. We now give, in the following, numerical details of the shear-layer simulations.

A plane shear layer which is discretized into one layer of vortex filaments has a characteristic vorticity thickness given by the filament core diameter of 2σ, and so we use the filament diameter as our reference length. As a result, $\sigma = 0.5$. By taking the circulation per unit length of the shear layer as the characteristic velocity, we can then render all velocities and times dimensionless.

In order to evaluate the Biot-Savart integral with second-order spatial accuracy, we represent the filament centreline by a cubic spline using the straight-line distance between the node points as the spline parameter. This allows us to determine the tangent vector at each node point, which presents an improvement over previous schemes using straight-line segments or circular arcs. In addition, the use of the spline formulation enables us to obtain a better representation of the locally induced velocity by subdividing filament sections close to a node in the process of calculating the self-induced velocity. Furthermore, the spline representation permits the easy introduction of additional nodes during the calculation in order to maintain a satisfactory resolution even when considerable vortex bending and stretching occurs. The filaments are repeatedly remeshed so that the arclength between successive nodes is always less than one but more than half of the initial core radius. In addition, the local curvature is determined and nodes are spaced in such a way that, within the above bounds, the product of the arclength between the nodes and the local curvature does not exceed $\frac{1}{8}\pi$. These criteria were established in order to provide an improved resolution of highly curved regions of the filaments without wasting numerical effort on the representation of scales too small to be accurately represented by our filament model. Their efficiency was checked by means of test calculations for a vortex ring. In the course of the simulations to be described, the number of nodes

increases approximately twice as fast as the total arclength, which shows that a considerable number of nodes are introduced for resolution of filament curvature.

Both the spatial and the temporal integration are carried out with second-order accuracy, with the node points being advanced in time according to a predictor–corrector scheme

$$\left.\begin{aligned} \boldsymbol{x}' &= \boldsymbol{x}(t)+\boldsymbol{u}(t)\,\Delta t, \\ \boldsymbol{x}(t+\Delta t) &= \boldsymbol{x}(t)+\tfrac{1}{2}(\boldsymbol{u}(t)+\boldsymbol{u}')\,\Delta t. \end{aligned}\right\} \tag{4}$$

The timestep is continuously adjusted so that the largest velocity component difference in $\boldsymbol{u}'$ and $\boldsymbol{u}(t)$ at any node point multiplied by the current timestep gives a length which is less than 2% of the initial core radius. In the course of the calculation to be discussed below, the timestep is reduced by approximately two orders of magnitude. In test calculations carried out for the model problem investigated by Siggia (1985), this predictor–corrector scheme proved to be as efficient as fourth-order Runge–Kutta time integration. At the same time, we prefer it to a multistep technique such as Adams–Bashforth, since we desire the ability to change the timestep at each step independent of previous timestep values. Since we do not have to use previous time level information, less work is required when we remesh a filament. We do not have to interpolate old velocities to new node point locations as the filament stretches and bends. Velocity values have to be stored for only two levels per node, so the total storage comes to nine times the number of node points (three spatial coordinates and six velocity components). Higher-order Runge–Kutta schemes with the same storage requirement are possible (Williamson 1980), but would require more computational effort. In vectorized calculations on a computer with no storage limitation, we precalculate the tangent vector at each node point from the spline representation. The integrand of the Biot-Savart law is evaluated in a nested loop which only examines each pairwise interaction once. We have not examined the possibility of treating those filament sections experiencing large acceleration (due to local rotation around neighbouring filaments) with a reduced timestep as compared to those filaments that are being convected at a large but steady speed.

In order to get a better understanding of how changes in the vorticity field affect the structure of the plane shear layer and to be able to compare our results to flow visualization experiments of Lasheras & Choi (1988), we also compute the evolution of the interface separating the two streams leaving the splitter plate. This is achieved by initially placing several hundred passive marker particles along straight lines in the spanwise direction between the two streams and then calculating their trajectories simultaneously with those of the vortex filaments. Depending on the local stretching, additional marker particles are introduced along these lines in the same way as nodes are introduced along the vortex filaments. In anticipation of the observed uneven stretching, the initial marker particle line density is larger in the region near the free stagnation point. For visualization of this interface we plot these marker particle lines as well as connecting lines at a constant spanwise spacing.

To obtain a problem that is numerically tractable, we limit ourselves to the analysis of a shear layer which is spatially periodic in two directions and develops in time. We lose the small asymmetry in the streamwise direction caused by the spreading of the mixing layer, but gain the ability to resolve more degrees of freedom in the nonlinear flowfield. The Biot-Savart evaluation of the velocity requires integration over all the vorticity in the flowfield, i.e. integration over all the periodic images of the control volume as well. For the two-dimensional case Nakamura *et al.*

(1982) use the analytic expressions for the summation over all images given in Lamb (1932). For the three-dimensional case, however, such an expression has not yet been found, so that we are forced to truncate the interaction to a finite number of images. Consequently, when evaluating the velocity of a node, we take into account the influence of each filament segment and its six closest images in the flow direction. This means that if x_{ij} denotes the closest distance between node i and node j and x_l represents the periodic length of the computational domain in the x-direction, then the interaction is evaluated for the seven distances that have x-components of $x_{ij}+nx_l$, where the integer n goes from -3 to $+3$ and includes 0, the closest image. Only the nearest segment image is considered in the spanwise direction, i.e. only y_{ij} is used. For the case of two layers of opposite vorticity there will be some long-range cancellation effects, and the number of images needed to achieve a certain accuracy is thus reduced. Furthermore, different levels of approximation to the various long-range interactions could be explored, but that will require further study in order to determine the appropriate parameter values.

In an incompressible viscous fluid, axial stretching of a vortex tube will reduce its cross-sectional area until a balance occurs between inward motion and outward viscous diffusion of vorticity. We have not included any increase of the core parameter due to viscous diffusion. A separate study of the viscous interaction of vortex rings yields vortex reconnection when sections of the rings with anti-parallel vorticity vectors approach each other (Ashurst & Meiron 1987). This topology change will not be considered in the present work as its occurrence is not likely during the early stages of the shear-layer evolution. In addition, we must remember that the isolated filament analysis indicates that our symmetric core parameter is not correct when the filament radius of curvature becomes comparable to the core size. Therefore, once a simulation has produced small-scale three-dimensional effects, continuation of the calculation demands some decisions. Should short-wavelength disturbances be calculated by replacing a single filament with many filaments at a much larger computational cost, or must we filter away short-wave effects and attribute this to viscous dissipation? At this time, we have not explored either approach.

In our simulation, the continued reduction of the timestep combined with the increasing number of node points leads us to stop the calculation as we approach diminishing returns in terms of advancing the problem time versus the computational cost per timestep. For example, when we start a calculation with 4050 nodes, the first timestep requires 48 s on a CRAY1, while the last timestep with 14700 nodes takes 500 s. However, as will be seen in the next section, this calculation has carried the shear layer well into the nonlinear regime.

3. Results

3.1. *The single shear layer*

We will begin by discussing the simulation in which we have discretized the flowfield into only one layer of vortex filaments in the (x, y)-plane (figure 1). This approach assumes that the second, weaker boundary layer emanating from the splitter plate quickly disappears through cancellation with part of the stronger boundary layer, so that the downstream evolution is determined by the global velocity jump alone, U_2-U_1. Even though we show in §3.2 that including both boundary layers results in closer agreement with experimental observations, we do see some of the basic shear-layer features in this simpler case with only one sign of vorticity. This means,

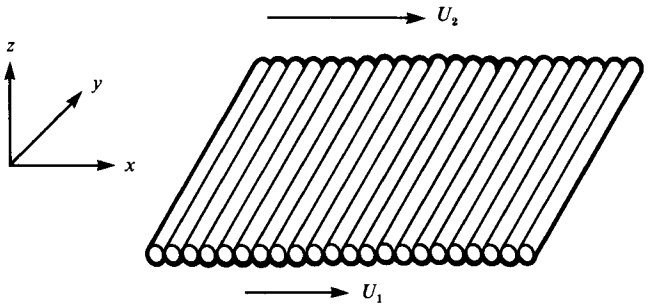

FIGURE 1. Discrete vortex filament representation of a shear layer with only one sign of vorticity. A smooth vorticity distribution is achieved when the filament core parameter is much larger than the filament spacing. The circulation of each filament is a function of the velocity jump U_2-U_1 and the filament spacing in the streamwise direction. The streamwise direction is in x, the spanwise in y, and the transverse direction in z.

however, that in the single-layer calculation, the velocity ratio of the two streams forming the shear layer is not uniquely defined, since an arbitrary constant velocity in the flow direction can be added. We will track the configuration of the filaments in a reference frame moving with the average velocity $\frac{1}{2}(U_1+U_2)$, so that only the velocity jump needs to be specified; the total circulation per unit length is U_2-U_1. Our control volume encompasses two wavelengths in the streamwise and three wavelengths in the spanwise direction. The vorticity layer is discretized into 99 filaments with initially 13 nodes each. In order to be able to compare our results to the experimental observations of Lasheras & Choi (1988) who impose periodic perturbations in the spanwise direction, we start our calculation with a sinusoidal dislocation of each filament centreline of amplitude 0.01. However, in contrast to their experiment, where the streamwise Kelvin–Helmholtz waves grow naturally, we also slightly force this instability with a smaller amplitude of 0.001. The initial perturbations consist of a displacement of the filament centres out of the plane of the vorticity layer. We chose the Kelvin–Helmholtz wave to have a length of 2π, which is about 1.4 times the length of the most amplified wave but in the wavenumber range where the discrete-vortex method duplicates the inviscid-stability-theory results. Based on experimental observations by Bernal (1981), we set the ratio of spanwise to streamwise wavelength to be slightly larger than $\frac{2}{3}$. The length and width of our control volume are 4π and 13.5, respectively.

In addition to the extra computational cost for carrying out three-dimensional calculations, there arises a great difficulty in comprehending the results. Looking at pages of numbers does not work, plotting velocity profiles is of some help, but the use of discrete-vortex methods requires further calculation for the determination of velocities. Drawing projections of the vortex filaments indicates which spatial volumes have intense vorticity, but still leaves the relations between filaments something of a mystery. Interactive graphical computing allows one to rotate and move dynamically through the data base and is the best means towards understanding (Zabusky 1981). Although slightly less convenient, computer-generated movies do produce the dynamical effect but usually require much effort to obtain just the right viewpoint to see what is happening in a particular region during a certain time period.

Given the restrictions of static figures, we attempt to explain the development of our shear layer, which was perturbed in the streamise and spanwise direction. Those

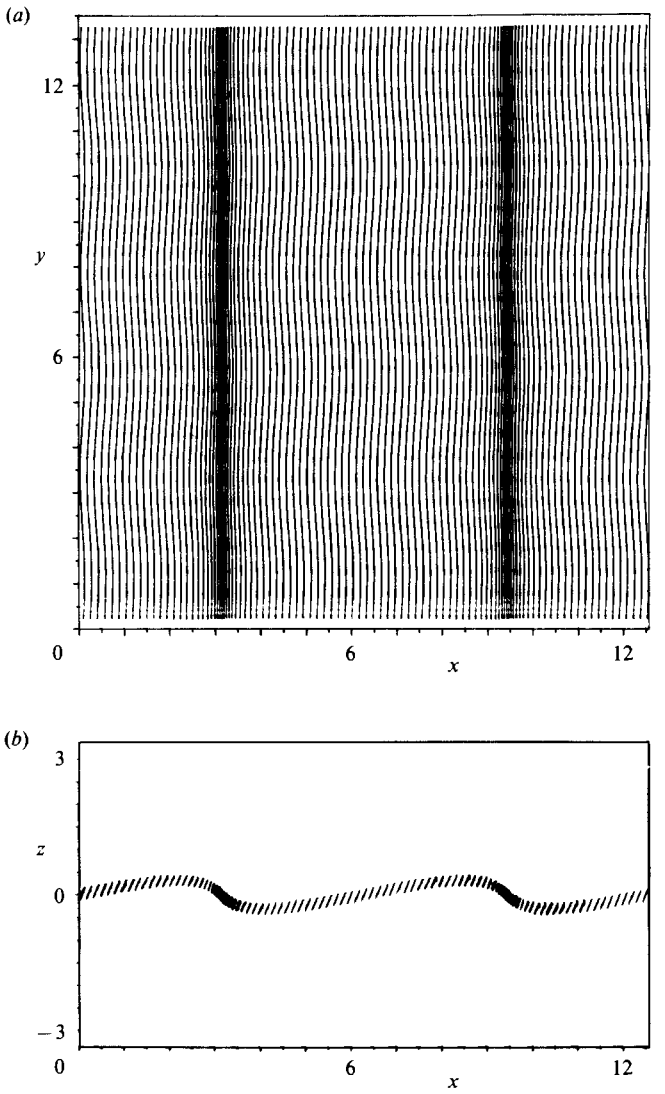

FIGURE 2. Top (*a*) and side views (*b*) of the single shear layer at time 117.5. The amplification of the streamwise wave leads to the formation of two regions of concentrated spanwise vorticity. The transverse vorticity component generated by the initial perturbation becomes tilted into the streamwise direction by the global shear.

nodes which, as a result of the initial spanwise perturbation, were displaced upwards into the faster stream, experience an acceleration in the flow direction, whereas those nodes initially displaced into the lower, slower stream are being decelerated. In this way, the global shear transforms the transverse component of the vorticity generated by the initial perturbation into a streamwise component, as can be seen in figure 2. The side view is a projection of the filament node point locations and the line length drawn in the side view indicates the excursion amplitude of the filament. This process, by which transverse vorticity evolves into streamwise vorticity, is also observed by Lasheras & Choi (1988) in their experiments (see their figure 19). At this time, the Kelvin–Helmholtz instability has begun to form two regions of concentrated vorticity, as seen in the top view, figure 2. In a coordinate system

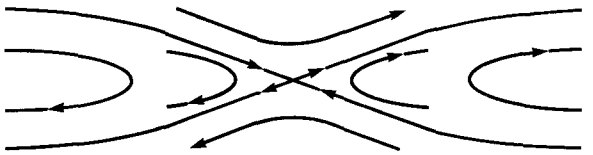

FIGURE 3. Qualitative picture of the streamline pattern in the (x, z)-plane between the spanwise rollers in a reference frame moving with the average velocity $\frac{1}{2}(U_1+U_2)$. The strain field in the vicinity of the free stagnation point leads to the stretching of the vortex lines.

moving with the two-dimensional rollers, this results in the formation of a local stagnation point in the braid region, the braid being the thinning vorticity region between the two-dimensional rollers. The stagnation point forms because outer fluid that is brought into the layer by the concentrated vorticity must divide into two streams: one winds around the upstream vorticity and the other one around the downstream vorticity. The nature of the strain field close to the free stagnation point is qualitatively sketched in figure 3. Hence filaments that cross the dividing stream surface in the stagnation region will undergo large amounts of stretching (a filament will cross these developing stream surfaces owing to the initial perturbations or, in the spatially developing mixing layer, owing to upstream disturbances).

As we proceed in time, the regions of concentrated vorticity develop into strong spanwise rollers, while the amplitude of the related strain field increases, figure 4. Further clustering or pairing of vorticity will not occur in the present calculation because we have not included any subharmonic disturbances (lower frequency, longer wavelength). We now have the situation analysed by Lin & Corcos (1984), namely the presence of alternating signs of streamwise vorticity in the thin braid region and subject to an outer strain field. As predicted by their analysis, the waviness of the filaments left in the braids grows as they undergo a continuing reorientation into the direction of the major strain axis (figures 4 and 5). This stretching is achieved by the vorticity becoming aligned with the extensional part of the strain field. The total length after time t is given as

$$l(t) = l(0) \exp\left(\int_0^t q(t)\, \mathrm{d}t \right), \tag{5}$$

where $q(t)$ is the time dependent strain along the filament. The maximum strain rate does not need to be much larger than the mean value in order to produce large stretching; it is the continuous application of strain along the vortex filament combined with the exponential weighting that increases the filament arclength.

While at time $t = 182.5$ we still observe a thin sheet of alternating streamwise vorticity, we find at $t = 245$, figure 6, which is the final state of our simulation, that this sheet has collapsed into concentrated vortices, again in agreement with the analysis of Lin & Corcos (1984). These concentrated streamwise vortices of opposite sign create regions of upflow and downflow across the layer. Since the vortex tubes move along with the fluid, they follow this motion, as can be seen in the front view, and this effect creates the appearance of wisps, seen in the side view. While in our simulation those filaments in the outer regions of the spanwise rollers show relatively little variation in the spanwise direction, the ones at the roller centre do clearly develop a spanwise undulation. This appears to be a manifestation of the core instability mode investigated by Pierrehumbert & Widnall (1982) which they called

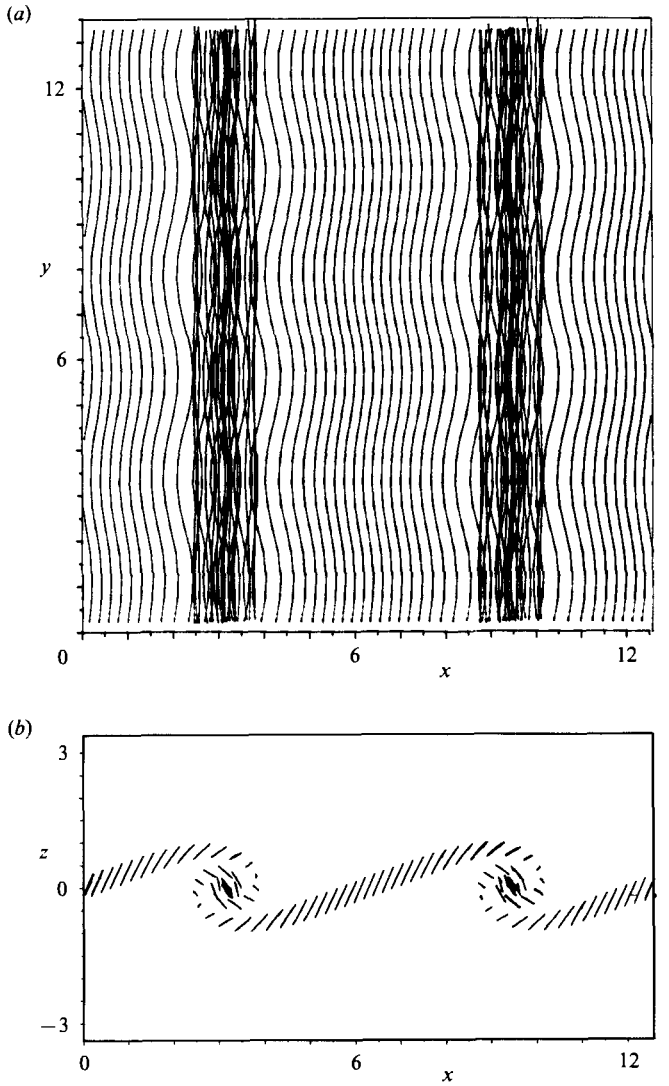

FIGURE 4. Top (*a*) and side views (*b*) of the single shear layer at time 145. The filaments located in the braids and in the centres of the evolving spanwise rollers experience the most stretching.

the translative instability. However, there are two major differences between their analysis and our simulations: they consider infinitesimal disturbances in the symmetrical Stuart type vortices and we follow the nonlinear evolution of vorticity given by the Kelvin–Helmholtz instability. As can be seen by comparing figures 4 and 5, the plane of the wavy filament centreline slowly rotates during the shear-layer roll-up process, and this counteracts the growth of the core instability into any one particular direction. This rotation effect reduces the three-dimensional distortion of the roller cores in comparison to the streamwise development seen in the braid region. At the end of our simulation, the roller cores have made a few revolutions and we see an 'out-of-phase' character in the streamwise vorticity components in that at those spanwise locations where a loop of braid vorticity points downstream, the roller-core has an upstream loop, see figures 4, 5 and 6. Likewise, the core streamwise

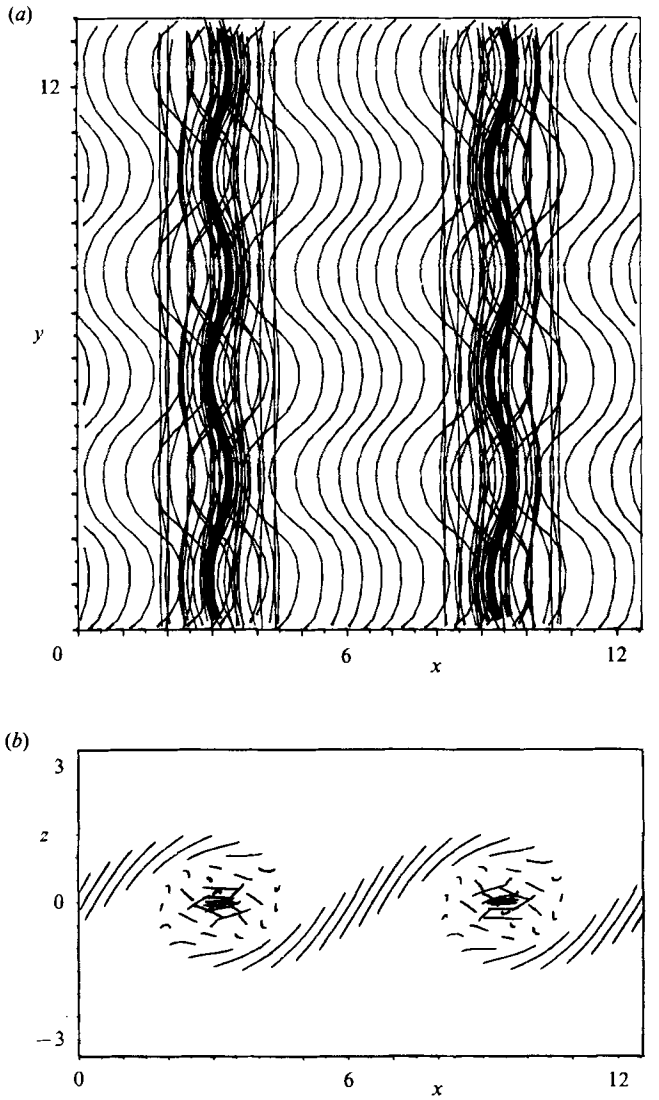

FIGURE 5. Top (*a*) and side views (*b*) of the single shear layer at time 182.5. The filaments located in the braid region have been stretched the most and are becoming aligned with the extensional strain direction.

vorticity points downstream at those spanwise positions where the braid streamwise vorticity points upstream. This 'out-of-phase' configuration is also observed experimentally by Lasheras & Choi (1988), and we will discuss it further in §4.

Since the present shear layer has only one sign of vorticity, it retains certain symmetry properties with respect to the flow direction as well as to the spanwise direction. This symmetry manifests itself in that the filament configurations are antisymmetric about the centre of the braids in the side view, and that the counter-rotating streamwise vortices have constant spacing in the spanwise direction. As we will see in the next section, these symmetry properties are changed by including a second, weaker layer of opposite vorticity.

In order to be able to compare our numerical results to flow-visualization

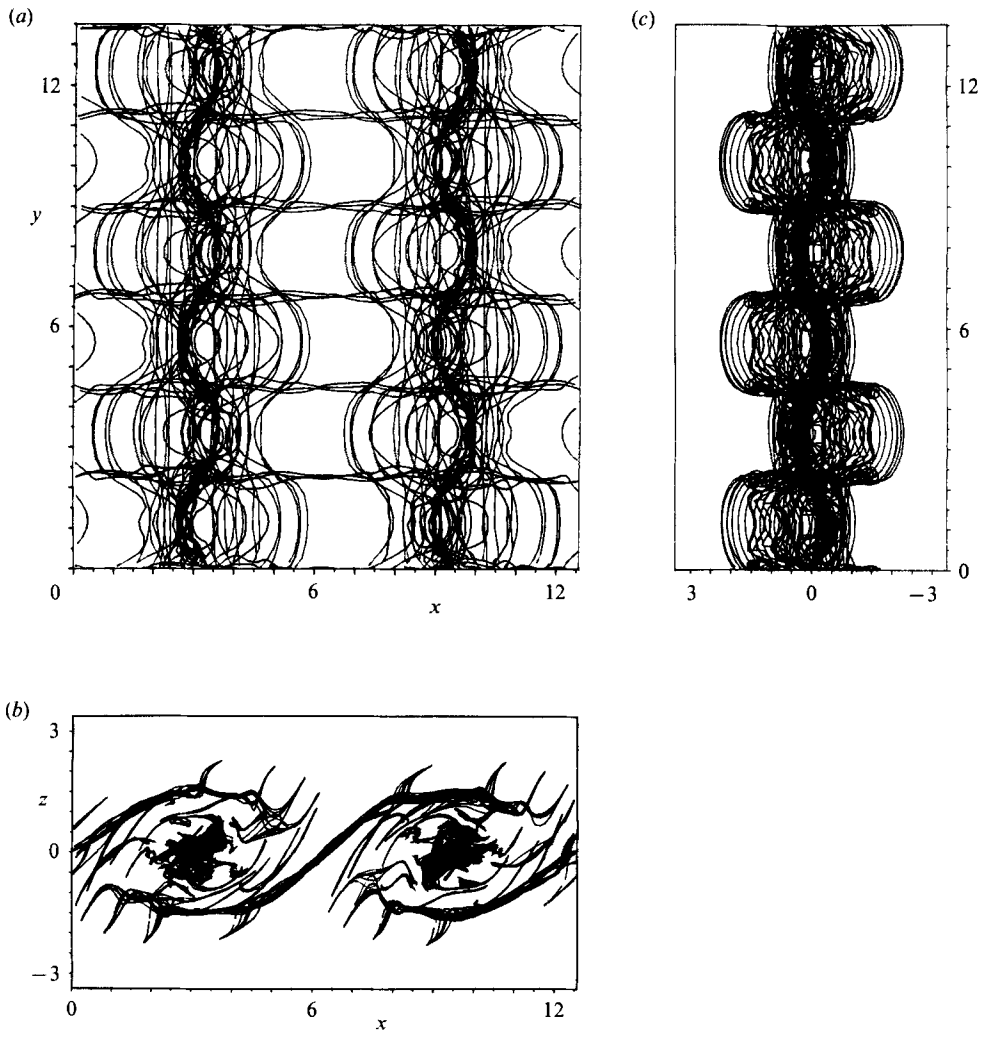

FIGURE 6. Top (*a*), side (*b*) and front views (*c*) of the single shear layer at time 245. The sheet of alternating streamwise vorticity has evolved into concentrated streamwise vortices equally spaced in the spanwise direction.

experiments, we have also plotted perspective views of an interface between the two streams forming the shear layer. For the present case with only one sign of vorticity in the flow, we have tracked the evolution of several hundred passive marker particles which represent a small section of the interface. Initially, this interfacial element is located at the edge of the rotational layer on the slow side and is close to the region where we expect the formation of the braid region with the free stagnation point. Consequently, this initially small area undergoes considerable stretching as it wraps around the roller cores, figure 7. The side view and the near upstream view at this stage of the simulation also show how the interface folds around the concentrated streamwise vortices in the braid region. The regions of upflow and downflow between these streamwise vortices can clearly be identified.

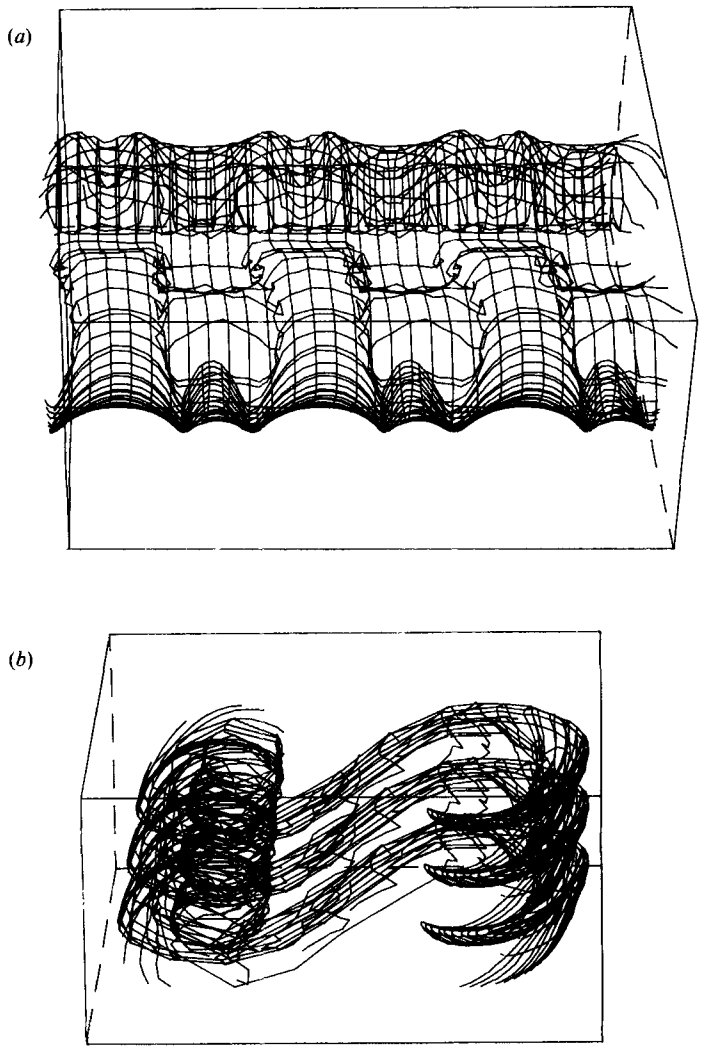

FIGURE 7. Perspective view of an initially small section of the interface located in the braid region in the centre of the control volume: (*a*) View from a near downstream direction. (*b*) Side view; the flow is to the right at the top and to the left at the bottom. The interface has become entrained into the spanwise rollers and also wraps around the concentrated streamwise vortices.

3.2. *Two unequal vorticity layers*

In order to obtain a more realistic representation of the mixing layer forming downstream of a splitter plate, we now consider the flowfield to be composed of two unequal boundary layers. Thus, by assuming that cancellation effects of the two opposite signs of vorticity are negligible during the initial stages of the mixing-layer growth, we define the free-stream velocities U_1 and U_2 and thereby the velocity ratio. This is in contrast to the previous simulation which used only one sign of vorticity.

The shear layers are represented by two layers of equal thickness in (x, y)-planes which have circulation of opposite signs: the upper layer with the negative circulation causes twice the velocity jump of the lower layer of positive circulation. Therefore, in the transverse direction the streamwise velocity changes by a factor of

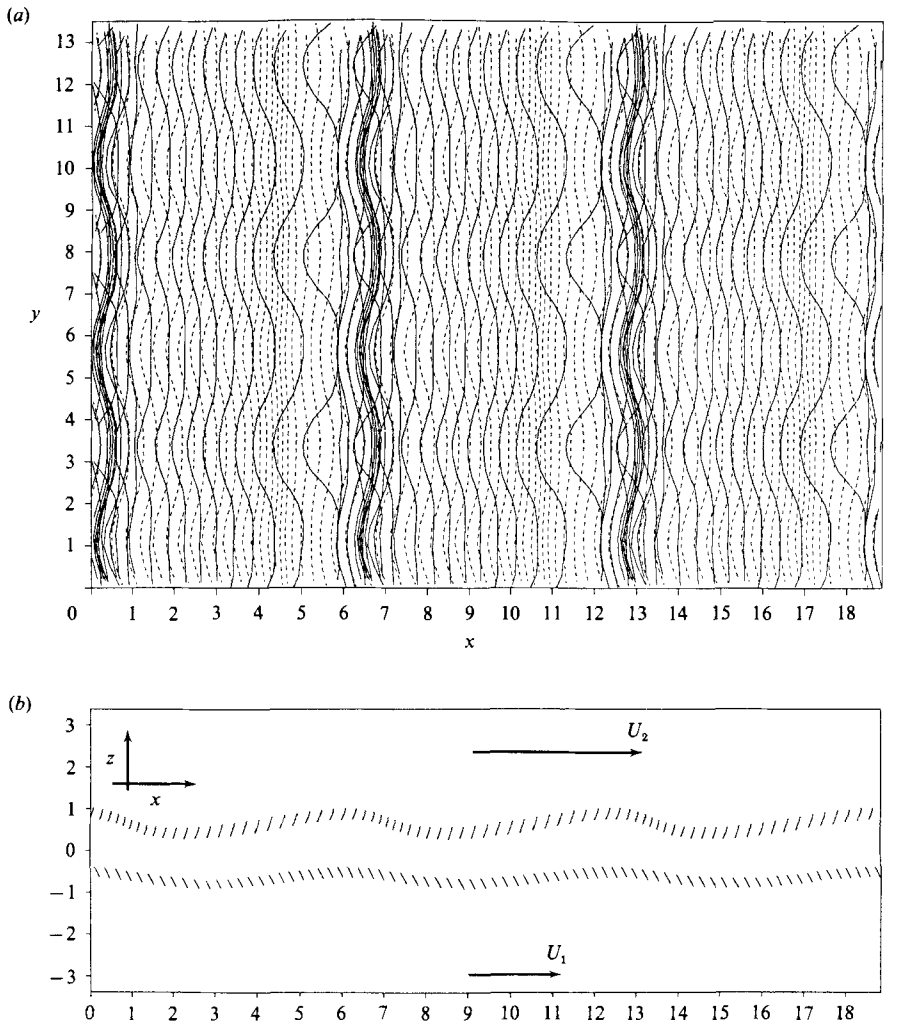

FIGURE 8. Top (*a*) and side views (*b*) of the two unequal shear layers at times 157.5 and 117.5, respectively. The upper vorticity layer (——) is of opposite sign and twice as strong as the lower layers (– – –). While the upper, stronger layer has already begun to roll up into concentrated spanwise vortices, the lower layer does not yet exhibit any clustering.

two, see figure 8(*b*). We have extended the control volume of the previous simulation so that there are three wavelengths in both the streamwise and spanwise direction (6π by 13.5). In the streamwise direction each vorticity layer is discretized into 75 filaments giving a spacing of $\frac{1}{2}\sigma$ in order to start with a smooth distribution of vorticity. Each filament initially consists of 27 nodes. The two layers are located at $z = \pm 0.65$, resulting in a slight overlap initially, so that the minimum velocity is 0.35 instead of zero. This means that we start our simulation at some location downstream of the splitter plate where the defect in the average velocity profile is already beginning to disappear. The initial perturbation is identical for both vorticity layers and is the same as in the single shear-layer case, namely a displacement of the filament centrelines out of the (x, y)-plane. The streamwise amplitude is 0.001 and the spanwise is 0.01.

At an early stage (figure 8), the upper, stronger layer (shown as solid lines) has already developed a slightly nonlinear character and is starting to form regions of concentrated vorticity, while the lower layer (drawn as dashed lines) still appears to be close to a linear wave. In figures 9 and 10 we present side views of each sign of vorticity separately since we cannot use different colours to distinguish between the filaments of positive and negative circulation. In addition, we have drawn several sketches of those particular filaments which exhibit the most stretching, see figures 11 and 12. In figure 9(*b*) we recognize that the stronger negative circulation clearly dominates the flow. It has formed spanwise rollers with a spacing equal to the initial streamwise perturbation wavelength. Filaments of the opposite sign of circulation have almost traversed the layer, as the strain pattern pulls them into the rollers. We must be cautious about the interpretation of how the two signs of vorticity intermingle, since we discretized the continuous sheets of vorticity but do not add new filaments in order to maintain a continuous vorticity layer. Thus, we face the possibility that the two signs of discrete vorticity may pass through each other during the course of the nonlinear motion. Increasing the number of filaments would decrease this effect, but it would also result in a much higher computational cost.

As in the single-layer calculation, we observe that the initial spanwise perturbation develops into alternating signs of streamwise vorticity. However, while in the one-layer case those filaments at the centre between two spanwise rollers experience the most stretching, we now find that the filaments with the strongest spanwise modulation are located closer to a downstream roller. In figures 9 and 10 we have labelled those filaments a and b. In figure 10 at time 226.25, filament a goes from the top of one roller to the bottom of the upstream roller, whereas filament b has remained in the braid region. Tracing these filaments in the top views is difficult, so we have drawn sketches of the development of these filaments. Figure 11 presents several views at two different times of just filaments a and b for better clarity. The curvature and sign of circulation of filament a at its largest z-location is such that it induces a velocity which moves filament b in the positive z-direction. This is also the direction in which the strong vorticity rollers wish to convect this flow region. The combination of all these factors results in a narrow vorticity structure with streamwise vorticity vectors alternating in sign. The spanwise distance of these structures is given by the initial spanwise disturbance wavelength, whereas the width of a single structure is only 1.5 units or one-third of the spanwise wavelength. The creation of these structures, along with their reduced core size due to filament stretching, results in large fluctuations in the z-velocity: a passive scalar would see narrow regions of upwelling surrounded by downward motion. In figure 9, we can see that filament a also pulls up sections of the opposite vorticity layer. In figure 10 these filaments add a further modulation to the z-velocity fluctuation.

As in the case of the single shear layer, for early times we observe an out-of-phase waviness of the cores of the spanwise rollers, figures 8(*a*) and 9(*a*). Towards the end of the simulation, however, the filaments of the weaker layer get pulled into the spanwise rollers and seem to destroy the very regular waviness of the cores, figure 10(*a*). This means that the change in the global strainfield caused by the weaker layer seems to affect the translative instability mechanism.

Sketches in figure 12 show the relative locations of the filaments with opposite signs of circulation in a part of the region occupied by filaments a and b. In particular, we are interested in the deformation of a Lagrangian interface between the high- and low-speed fluids. As the stronger vorticity forms the two-dimensional roller, some of the weaker filaments are also pulled into the roller, as described above

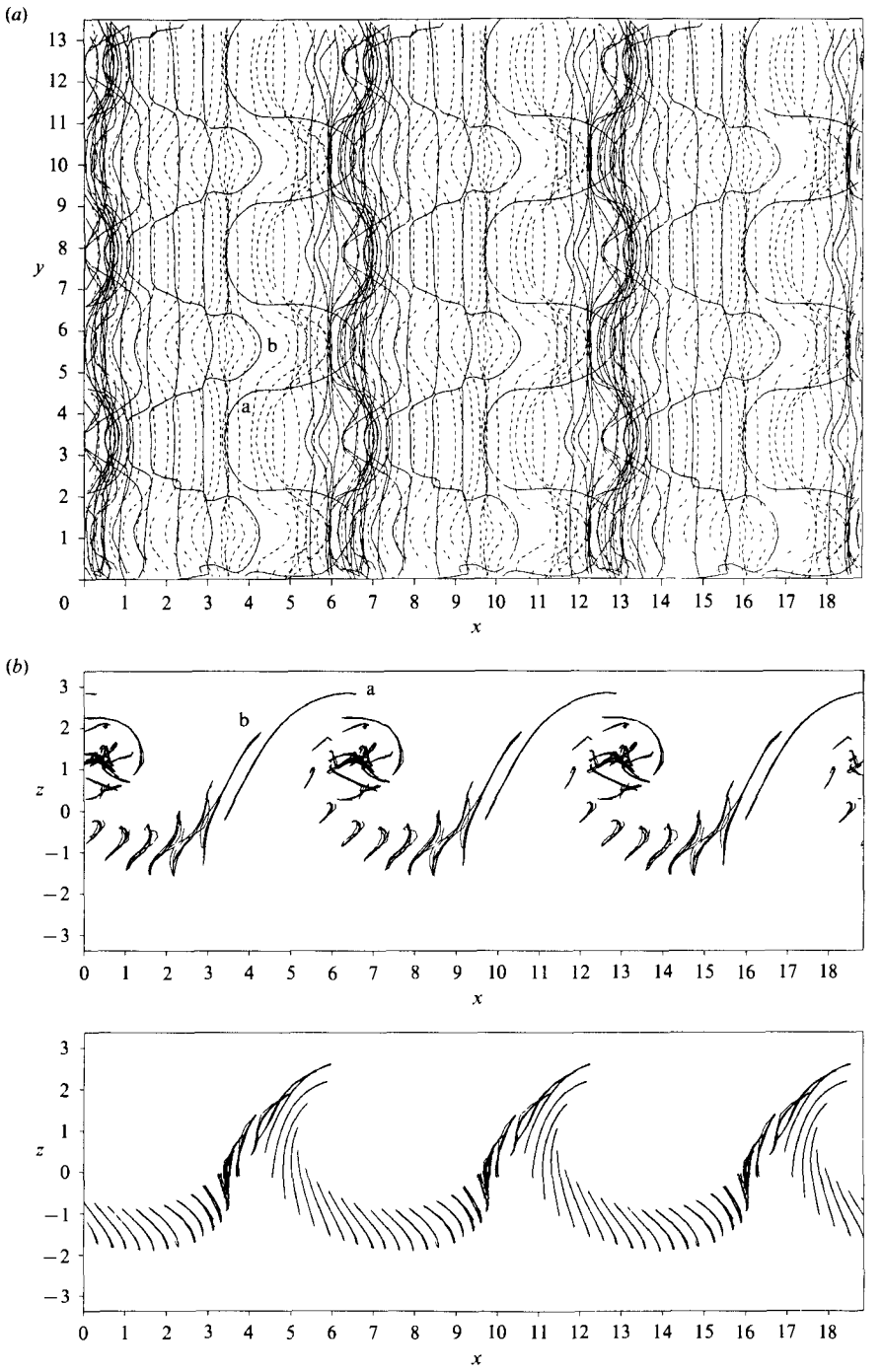

FIGURE 9. Top (*a*) and side views (*b*) of the two unequal shear layers at time 191.875. Side views are presented separately for the upper, stronger layer and the lower, weaker layer. Notice how the stronger layer forms spanwise rollers as a result of the Kelvin–Helmholtz instability, and how the filaments marked a and b undergo large streamwise stretching. The weaker layer experiences a more uniform stretching and becomes partly entrained into the spanwise rollers, so that both signs of vorticity can be found at almost any transverse coordinate between the maximum and the minimum values.

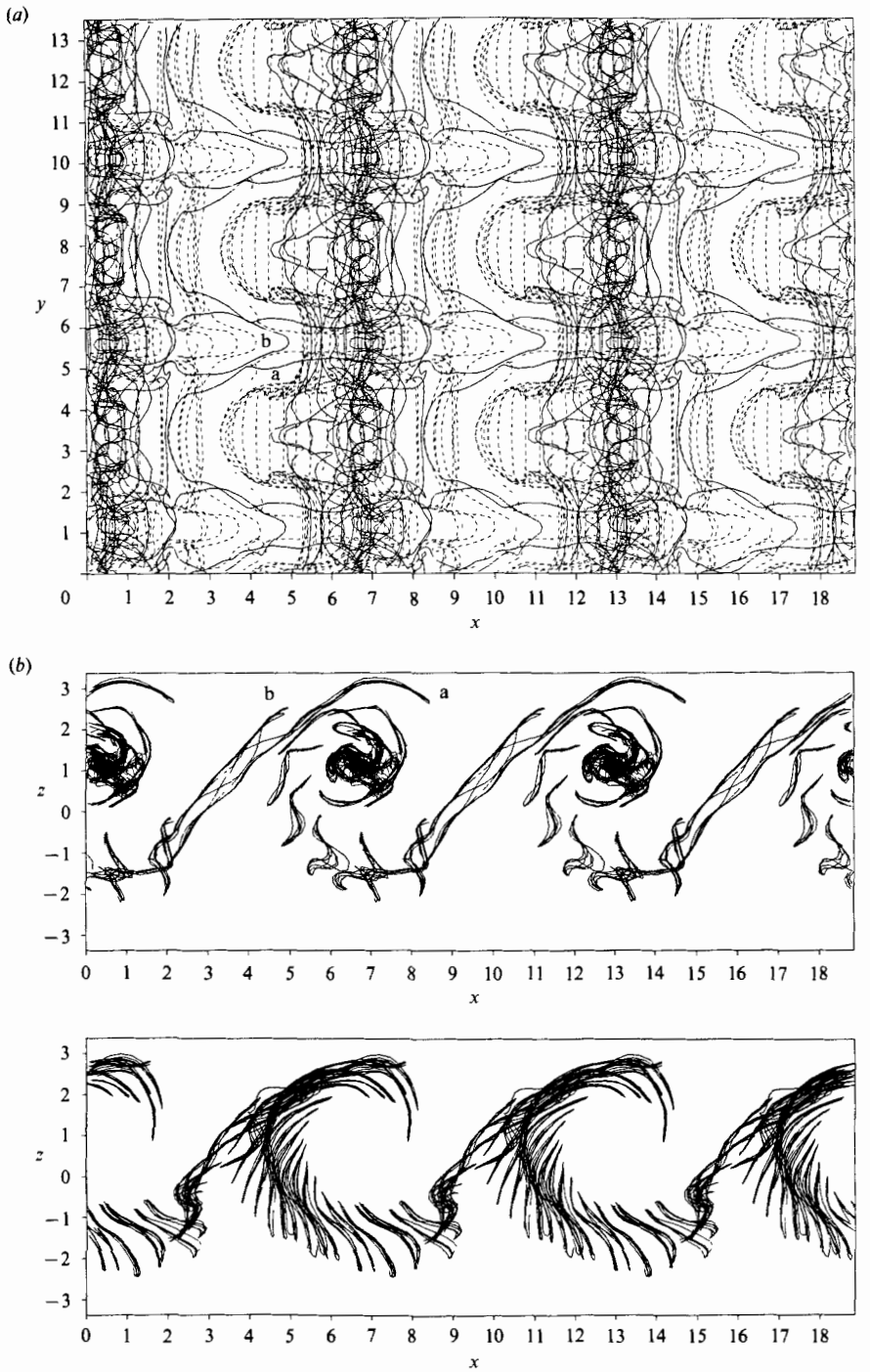

FIGURE 10. Top (*a*) and side views (*b*) of the two unequal shear layers at time 226.25. In the upper, stronger layer of vorticity the section of the braids undergoing the strongest stretching is not located at the centre between the rollers as in the one-layer simulation, but closer to the downstream roller. The filament marked a is now stretched from the top of one roller to the bottom of the upstream roller. Some of the weaker filaments of the lower layer wrap around the spanwise rollers. Since no subharmonic perturbations were introduced initially, we do not observe a pairing mode.

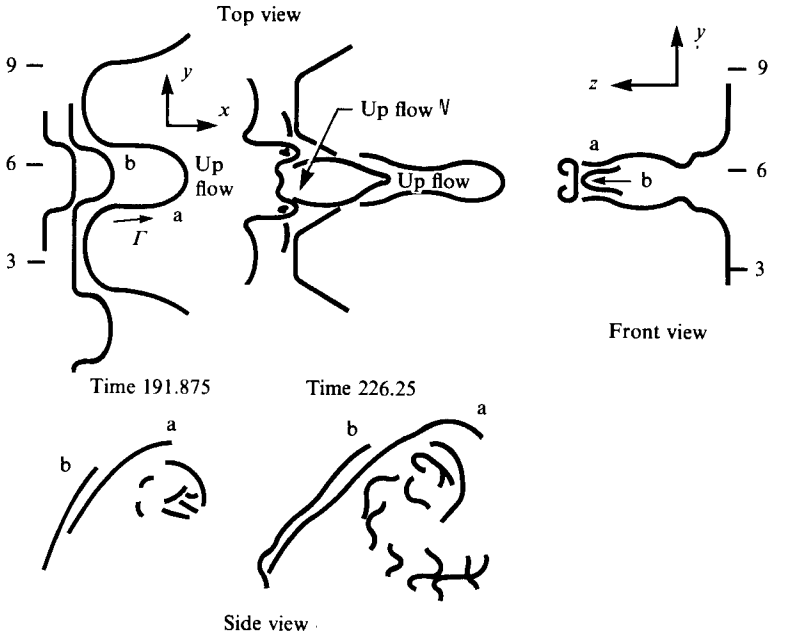

FIGURE 11. Sketches of filaments a and b at the times of figures 9 and 10 from different views.

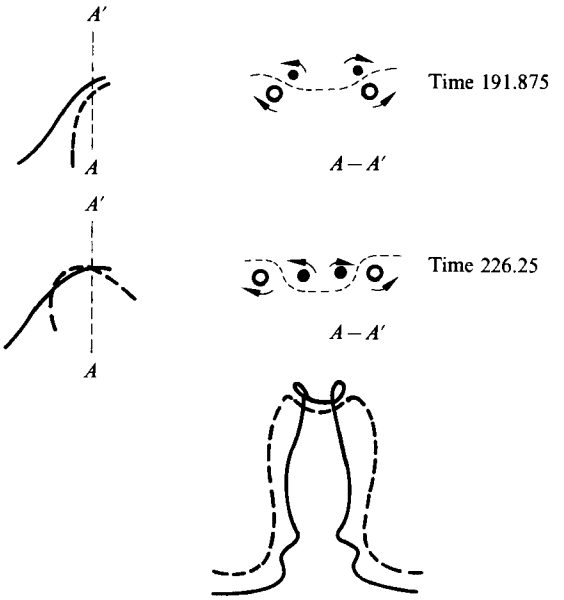

FIGURE 12. Relative locations of the two signs of circulation during the formation of the streamwise structures sketched in figure 11. In views of the section A–A' the stronger negative circulation is shown by filled circles. Because these filaments loop into and out of plane A–A', each filament type exhibits both directions of rotation. The front view indicates the reduction of the spanwise separation of the 'legs' of the positive filaments.

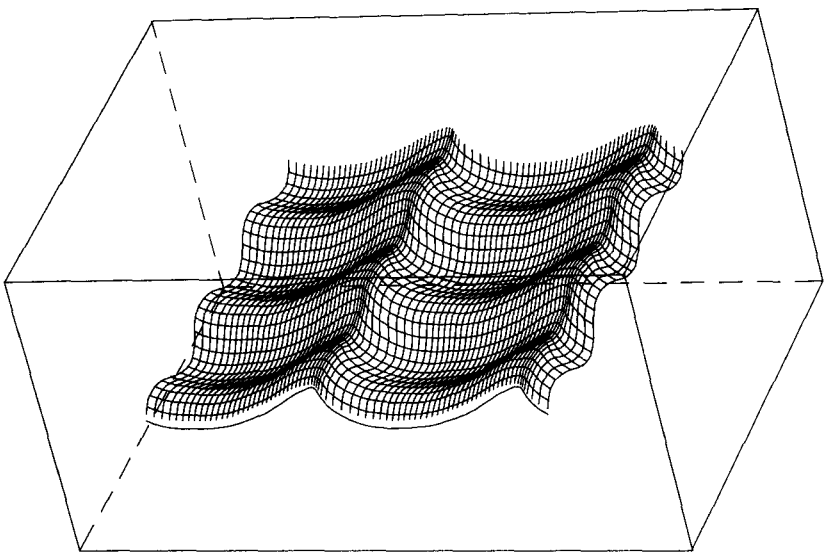

FIGURE 13. Perspective near top view of the interface separating the two unequal shear layers of opposite sign at time 141.25. The flow is from left to right. The shape of the interface reflects the growth of the two-dimensional Kelvin–Helmholtz instability as well as the spanwise modulation due to the evolving streamwise vorticity.

and sketched in figure 12. As a result, weaker filaments get reoriented in such a way that they develop a component of vorticity pointing in the circumferential direction of the spanwise rollers. Now in the region above the centre of the spanwise roller ($z > 2$), the weaker filaments move up and the stronger one moves down, producing a folding in the interface as shown in figure 12. In the lower region ($z < 1$), the stronger filaments reduce the spanwise separation between the 'legs' of the weaker filaments which causes the lower layer to look like a mushroom shape in the top view, see figure 10(*a*).

The evolution of these narrow structures spaced relatively far apart in the spanwise direction is also visible in the perspective views of the computed interface. At time $t = 141.25$, the perspective view in figure 13 shows that the interface has developed a wavy deformation in both the streamwise and the spanwise directions, with a crest forming where it is being pulled into the evolving spanwise roller. The deformation in the spanwise direction at this time still resembles a sine wave, since the nonlinear evolution of the vorticity field has not yet produced the narrow streamwise structures. At a later time $t = 160.0$, however, their presence is reflected by the interfacial shape, figure 14. Short arcs in the regions of upwelling fluid are connected by long gentle arcs where the fluid is being displaced downwards. The modulation of the flow in the spanwise direction also becomes obvious from the fact that at different spanwise positions the interface is being pulled into the rollers at different rates. So if we look at the flow from the top (figure 15), the 'overlap' of the interface is much more pronounced at some positions than at others. All of these features can also be seen in flow-visualization experiments of Lasheras & Choi (1988), thus strengthening our confidence in the numerical simulation. Comparison of the experimental and numerical interfaces at later times, however, requires a more sophisticated hidden line-plot routine, and in addition it should be based on cuts through the interface along all three axes in order to extract the information

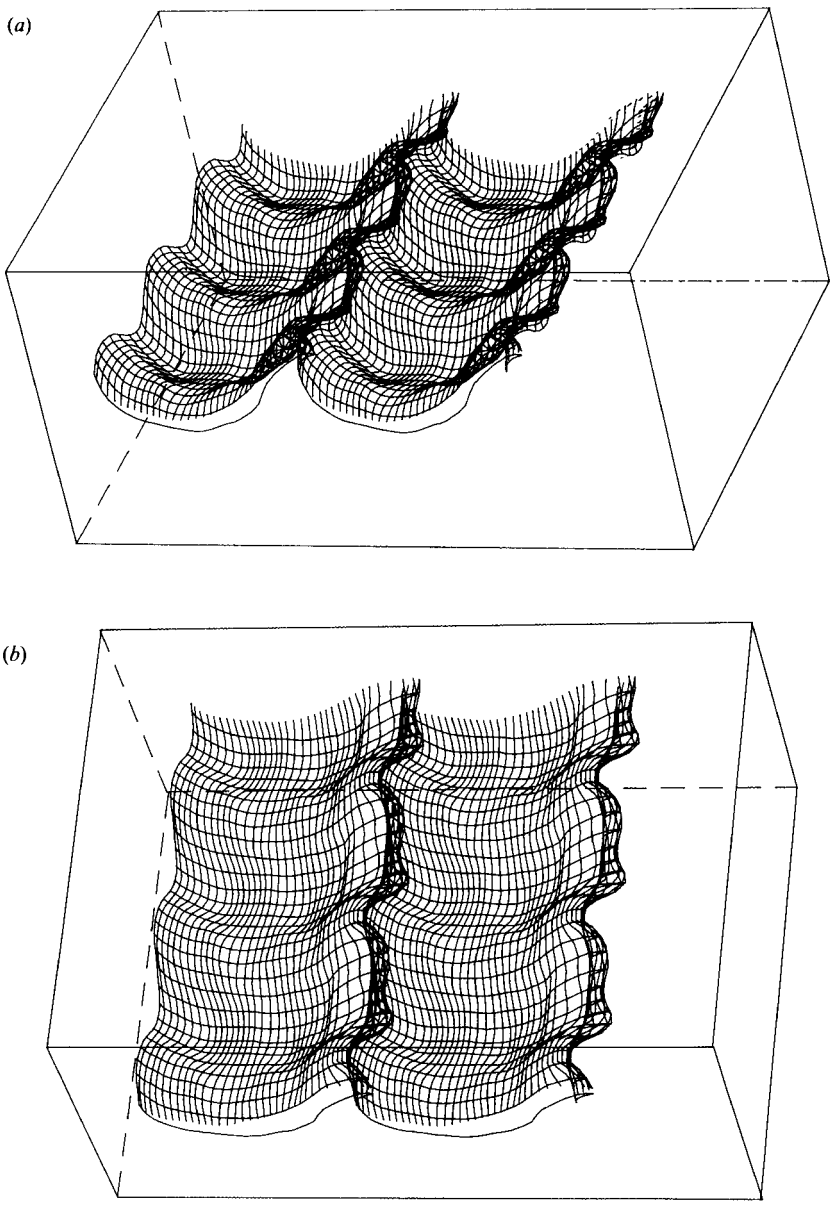

FIGURE 14. Perspective view of the interface separating the two unequal, opposite shear layers at time 160.0. (*a*) Near-side view; the flow is from left to right. (*b*) Near-top view; the flow is from left to right. At this time, the interface has begun to wrap around the spanwise rollers. In the spanwise direction it shows long, gentle arcs between the streamwise vorticity structures and short arcs at the locations of the streamwise vortices. The waviness of the interface in the spanwise direction indicates regions of upward and downward motion.

necessary for the identification of the interface dynamical evolution. We have started such an investigation (Meiburg & Lasheras 1986).

Some of the highly nonlinear motion described above may be sensitive to how many filaments are used to discretize the initial vorticity layer. In particular, the braid region is depleted of vorticity by the two-dimensional strain field of the

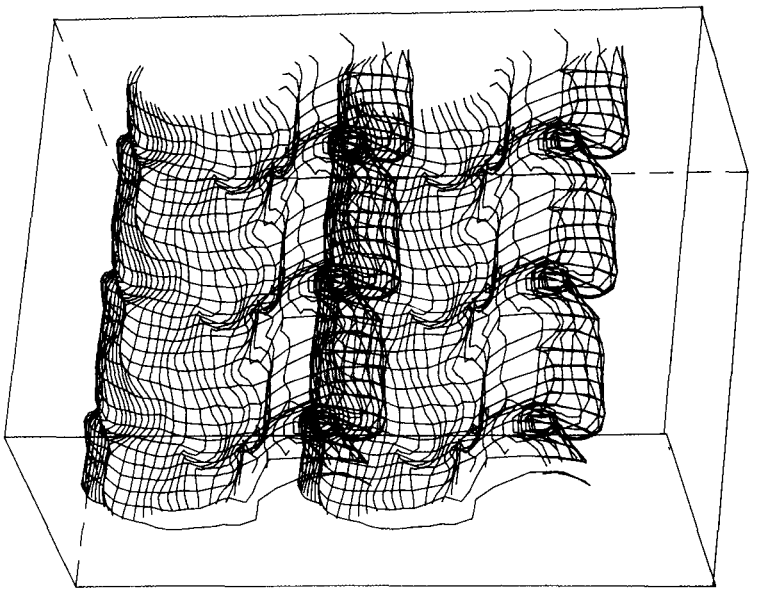

FIGURE 15. Perspective near top view of the interface separating the two unequal shear layers at time 178.75. The flow is from left to right. The interface wraps around the spanwise rollers between the locations of the streamwise vortices and thus generates a 'tongue' structure in the top view.

Kelvin–Helmholtz instability and thus in future simulations more, but weaker, filaments could be inserted in the braid region compared to the region that becomes the core.

The interface and the filament configuration for the case of the single-vorticity layer (figure 7) do not show the asymmetry in the streamwise and spanwise directions observed in the two-vorticity layer simulation. This shows that the formation of the narrow streamwise structures found in experiments and calculations is a result of the nonlinear interaction between the two-vorticity layers. The loss of symmetry in the two-layer calculation is related to the enhancement and reduction of relative streamwise displacements for filaments in the stronger layer by the addition of the second layer of vorticity. Stronger-layer filaments with initial transverse perturbations respond differently to the effect of the weaker vorticity depending on their streamwise location with respect to the free stagnation point, see figure 8. It appears that the three-dimensionality occurs first in the downstream half of the braid region. Another significant difference in the two calculations is the spanwise spacing of the streamwise vorticity: the single layer produced alternating streamwise filaments spaced at half of the initial disturbance wavelength, whereas in the two-layer calculation the weaker vorticity produces a nonlinear effect and creates structures of spanwise width equal to one-third of the initial wavelength and without streamwise symmetry.

3.3. *The effect of localized spanwise perturbations*

Lasheras *et al.* (1986) generated streamwise vorticity by a single localized disturbance on the splitter plate and they observed a flow pattern downstream of the splitter plate which is similar to the pattern seen in naturally growing mixing layers or in mixing layers with imposed periodic spanwise perturbations. Lateral spreading of the localized streamwise structures occurs during the two-dimensional roll-up and

pairing process. Aref & Flinchem (1984), approximated these conditions by numerically studying a single-vortex filament with its velocity dependent only on filament curvature and imbedded this filament in a uniform shear field. They found that an initial disturbance of the filament, corresponding to a soliton, generates spanwise wiggles with a spacing of $\lambda = (\Gamma L/U)^{\frac{1}{2}}$ where U/L is the applied shear and Γ is the circulation of the filament. Pierrehumbert (1986) shows that the linear stability characteristics of this filament model yield a dynamical evolution similar to that resulting from the full nonlinear dynamics considered by Aref & Flinchem. The self-induced rotation of disturbances and the applied shear give a preferred wavelength for maximum growth, the same wavelength as empirically determined by Aref & Flinchem. Only filaments with rotation in the same sense as the imposed shear will experience exponential growth of disturbances; filaments of opposite circulation are also unstable but not exponentially, and hence the selection of a preferred wavelength is not so evident. Both of the calculations result in asymmetric wave shapes which may be caused by the self-induced translation of a helically twisted filament.

The above-mentioned experimental and theoretical observations indicate that a localized perturbation under the influence of a global shear spreads out in the spanwise direction in an almost periodic fashion, so that it ultimately leads to a configuration similar to that caused by a periodic disturbance. We have attempted to simulate numerically the effect of a local perturbation when the filament dynamics are determined by the full Biot-Savart integral. For that purpose, we perturbed all the upper-layer filaments in a spanwise region centred around the middle of the spanwise coordinate, y. The perturbation is a displacement in the transverse direction over the positive part of a sine wave, i.e. the disturbance wavelength is λ_d and the spanwise extent of the disturbance is half of λ_d.

In the simulation shown in figure 16(*a*), λ_d is 4.5 and the sine wave amplitude is 0.001. This small amplitude was used because the discontinuous filament curvature generated strong three-dimensional effects and hence required a large number of nodes. In a second calculation, shown in figure 16(*b*), λ_d is 13.5 and we took the cube of a sine wave with amplitude 0.01. The main difference between these two simulations lies in the smoother curvature distribution of the cubic. Since the two-vorticity layers have a separation of 2.6 core radii in the transverse direction, we can consider them to be initially independent of each other. In both simulations we observe that the filaments of the stronger layer develop large distortions, while those of the opposite weaker layer remain almost straight. Since we perturbed all the filaments of the stronger layer in an identical fashion, isolated filaments in a uniform shear field, as analysed by Aref & Flinchem, do not appear in our simulation. From several computer runs, we find the scale of the spanwise response to be independent of the disturbance wavelength λ_d, the initial amplitude, and the details of the initial wave shape. Rather we observe the rapid growth of wiggles at those locations along the filaments where the initial perturbations caused the largest curvature. In order to determine if the spanwise development could be given by $(\Gamma L/U)^{\frac{1}{2}}$, we also carried out runs in which we varied the shear rate U/L, or the filament circulation, Γ. With a constant shear rate, we made runs with filament circulation either twice or half the value used in figure 16 and did not observe any change in the dominant pattern that is seen in figure 16. Reduction of the shear strength was achieved by doubling the vortex-core diameter as well as the initial distance between the two-vorticity layers. The resulting structures have a width which is essentially twice that shown in figure 16 and thus scales with the change in the core parameter.

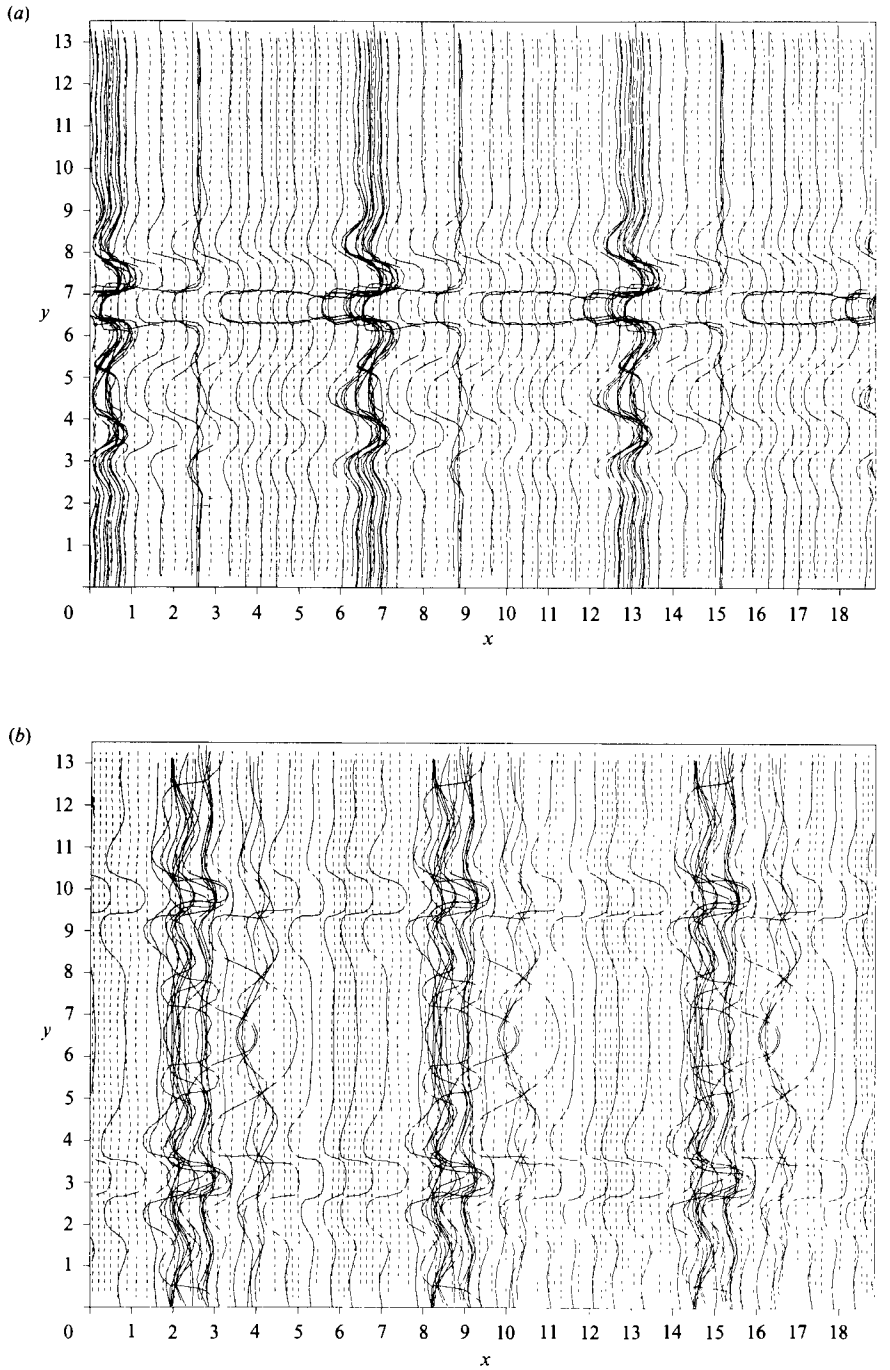

FIGURE 16. Filament configuration when the initial perturbation is limited to a finite region. (*a*) The region between $y = 5.625$ and $y = 7.875$ was initially perturbed with the positive half of a sine wave, λ_d is 4.5 and the amplitude is 0.001 (time 137). (*b*) The region between $y = 3.375$ and $y = 10.125$ was initially perturbed with the positive half of the cube of a sine wave, λ_d is 13.5 and the amplitude is 0.01 (time 156.25). In both cases the spanwise response appears to exhibit the same wavelength, which is a small multiple of the filament core radius.

In all cases, the spanwise response appears to exhibit a wavelength that is a small multiple of the core radius. Hence we cannot exclude the possibility that the spurious short wavelength instability of our filament model determines the spanwise scale evolving from these localized disturbances. Unlike the simulations considered in this section, the initial periodic spanwise disturbances described in §§3.1 and 3.2 do not contain curvature discontinuities, and thus they do not initially excite the short-wavelength response. Rather they lead to a smooth evolution of the flowfield, in which vortex stretching ultimately leads to highly curved vortex filaments. Since in the long-wavelength limit the stability characteristics of the filament model are correct, we have more confidence in the early three-dimensional development of the periodic disturbances than in the short-wavelength response shown in figure 16. It is not entirely clear at this point what might constitute the best way to simulate small-wavelength perturbations with the vortex dynamics technique.

4. Comparison with experimental observations

While we have carried out a numerical investigation of the evolution of a temporally evolving shear layer with an imposed periodic spanwise perturbation, Lasheras & Choi (1988) have investigated experimentally a spatially growing mixing layer with similar perturbations. The ratio of free-stream velocities in their experiments is approximately 2.27 as compared to 2.0 in our simulation. They introduce periodic spanwise perturbations by giving the trailing edge of the splitter plate a sine wave modulation either in its own plane or in a plane perpendicular to the plate. Using laser induced fluorescence as well as direct interface visualization, they develop a detailed picture of the two- and three-dimensional processes which determine the early stages of the mixing-layer growth. As we will see, a comparison of the numerical and the experimental results shows good agreement and contributes to a more complete understanding of the evolving flow patterns.

Both the experiment and the numerical simulation are dominated initially by the growth of the two-dimensional Kelvin–Helmholtz instability, which leads to the roll-up of the layer and the formation of spanwise rollers. During this phase, the global shear tilts the transverse vorticity component, which was introduced by the initial perturbation, into the flow direction. This can be seen in the side views presented in figures 2 and 8 and is also sketched in Laheras & Choi (1988), figure 19. The evolving two-dimensional strain pattern leads to the intensive stretching of this streamwise vorticity component in the vicinity of the free stagnation points. In this process, the braid vorticity reorients itself along the major axis of the strain field and develops a strong streamwise component. As a result, the wave crests evolving during the roll-up of the interface begin to show a spanwise modulation visible both in the simulation (figure 13) and in the experiment (Lasheras & Choi 1988, figure 6). As we proceed in time, the experiment shows the formation of narrow streamwise structures of counterrotating vortices, although the initial perturbation had been of sinusoidal character. Thus, we see the same nonlinear behaviour that we also observe in our simulation employing two signs of vorticity, figure 10. The equal spacing of the counterrotating streamwise vortices displayed by the simulation neglecting the weaker boundary layer (figure 6), is not seen in the experiment. Both in the experiment and in the two-layer calculation we find that at the spanwise locations of the streamwise vortices the interface entrainment is reduced in comparison to locations between the streamwise structures. Looking at the interface from the top, we observe the formation of 'tongues' where the interface wraps around the spanwise

rollers between the streamwise structures (figure 15 and Lasheras & Choi, figure 14). This demonstrates the impact of the three-dimensional structure on the growth of interfacial area.

Lasheras & Choi conclude from their flow-visualization experiments that the streamwise structures always originate in the braid region, and on the basis of our simulations we can confirm that statement. In the braids we see the situation of a sheet of streamwise vorticity of alternating signs which then experiences strong stretching in the strain field of the spanwise rollers. The initially nearly spanwise vorticity aligns itself with the major axis of strain and ultimately collapses into concentrated vortices. This confirms the analysis given by Lin & Corcos (1984) and Neu (1984). On the other hand, the translative instability of the roller cores suggested by Pierrehumbert & Widnall (1982) appears to grow only during the very early stages of the flow. A moderate out-of-phase waviness of the roller cores is observed both in the numerical simulation (figures 5 and 6), and in the flow visualization (Lasheras & Choi, figure 13). However, during the later stages it seems that the slow continuous rotation performed by the roller cores in the process of the roll-up counteracts their instability, and neither the experiment nor the simulation exhibits any further growth of the core pattern. In general, our numerical results as well as the experimental observations of Lasheras & Choi resemble much more closely the pattern of alternating signs of streamwise vorticity inferred by Bernal (1981) from laser sheet illuminations.

Jimenez, Cogollos & Bernal (1985) record mixing information on films via laser induced fluorescence of a dye added to the low-speed flow. The laser light is introduced in a sheet normal to the flow direction in order to examine the three-dimensional structure. They present perspective views of what they deduce to be counterrotating vortices, and attempt to estimate the streamwise circulation from the geometry of the interface in the braid region. By balancing the strain effect of the two-dimensional vorticity with the induced velocity from the alternating streamwise structures, they estimate the circulation ratio to be 0.6 ± 0.8 (streamwise over spanwise circulation; the large uncertainty is caused by the small sample of 23). In the spanwise direction they determine the interface amplitude to spacing ratio to be 0.6 ± 0.2, a value which corresponds to the one that we observe during the late stages of our interface simulation. From this ratio their model predicts, for our conditions, a circulation ratio of 0.64. In our calculation there are sixteen filaments wrapped into the core region, and thus there should be ten filaments pointing in the stream direction. At this stage of the calculation we only see two filaments of the strong layer, and depending on the x location, one to four filaments of the weaker layer (figure 10). While our discretization of this region at the final simulation time has become relatively poor and our calculated flow has not undergone any pairings of the two-dimensional rollers, we see a very complex structure emerging in the stream direction that is not a simple counterrotating vortex pair. Hence, the circulation estimates based on interface shape may not be very realistic. We have to keep in mind that the experimental information does not directly visualize the vorticity but instead records the interface of a scalar which is convected by the vorticity, and the actual structure may be much more complex than simple alternating signs of concentrated vorticity.

5. Conclusions

We have presented a numerical study of the evolution of the two- and three-dimensional instabilities in the plane shear layer. Knowledge of these instability mechanisms and the evolving structures is required in order to obtain any control over chemical reactions in such a flow. By means of Lagrangian vortex dynamics simulations we have been able to give a detailed description of the early two- and three-dimensional stages of the shear-layer development that results from given initial disturbances. Our calculations show that the concentrated streamwise vortices originate in the braid region between the spanwise rollers, whereas the translative core instability does not grow beyond small amplitudes.

While a single-layer simulation leads to certain symmetry properties of the flowfield both in the streamwise and in the spanwise direction, the inclusion of a second, weaker vorticity layer of opposite circulation eliminates this symmetry. From a comparison of our results with the flow visualization experiments of Lasheras & Choi (1988) we conclude that both boundary layers emanating from the splitter plate should be included in a mixing-layer simulation. Only by doing so can we observe the evolution of the narrow streamwise structures seen in the experiment. A further important conclusion to be drawn from the vortex dynamics simulations is that the processes dominating the early stages of the mixing-layer development can apparently be understood in terms of essentially inviscid vortex dynamics.

Our simulations do not reveal any single disturbance which causes 'the' three-dimensional instability of the plane mixing layer. From the experimental work, it appears that the origin of the streamwise vorticity lies in any upstream disturbance that creates vorticity with components other than in the spanwise direction. The mutual induction of non-spanwise vorticity and/or the stretching effect of the mean shear velocity will intensify any non-zero streamwise vorticity when viscous effects are small.

In comparison with Eulerian finite-difference or spectral techniques, the Lagrangian vortex method has advantages and disadvantages. The Lagrangian scheme as a natural adaptive mesh presents a distinct advantage for unbounded flows, whereas in a wall-bounded flow it is clear where an adaptive fixed mesh should concentrate the grid points. The grid-free Lagrangian method avoids the artificial diffusion introduced in grid convection schemes, but time integration errors in the Lagrangian trajectories may contribute to an artificial growth in the second moment of a vorticity distribution described by a collection of discrete vortices. We know that the assumption of a constant vortex core shape violates local strain effects, but there is a corresponding problem present in Eulerian solutions of the Navier–Stokes equations, where the strain field may create structures that diminish in size and cannot be resolved on the selected mesh spacing. Of course, the use of more node points in either method will reduce this effect but will also increase the computational cost. For research purposes, we feel that the Eulerian and Lagrangian methods complement each other and the advantages of each method should be exploited by appropriate application.

The current algorithm uses continuous filaments described by cubic splines with second-order integration in space and time. This numerical scheme presents an improvement over previous work using straight segments between node points. Even so, the calculations have only been carried out until the initial filament arclength doubled. At this point we reach the limit of the present scheme due to the diminishing timestep and the increasing number of node points. In order to be able

to continue the flow further into the nonlinear regime, the method needs to be changed in several ways: (i) the filaments could be filtered in space to remove sections where the radius of curvature is less than the core radius; (ii) a local timestepping variant could be developed, i.e. regions where filaments experience large rotation rates, and hence acceleration, could be treated separately in order not to reduce the timestep for all node points; (iii) the Biot-Savart interaction could be split into long- and short-range effects in order to decrease the square dependence on the number of node points, and (iv) further development is needed in the core model and its implications for short-wavelength disturbances and energy conservation.

The authors would like to acknowledge the frequent helpful discussions with J. C. Lasheras. The analysis of our results greatly benefited from the opportunities of discussing them in the light of experimental findings. Discussions with A. Leonard and Gregoire Winckelmans on some of the numerical aspects have also been very helpful in this work. This work was partially carried out while E.M. was a Ph.D. student at the Institut für Theoretische Strömungsmechanik, DFVLR, D-3400 Göttingen, West Germany. This work was partially supported by the United States Department of Energy, Office of Basic Energy Sciences, Division of Chemical Sciences.

REFERENCES

ANDERSON, C. & GREENGARD, C. 1985 On vortex methods. *SIAM J. Numer. Anal.* **22**, 413.

AREF, H. & FLINCHEM, E. P. 1984 Dynamics of a vortex filament in a shear. flow. *J. Fluid Mech.* **148**, 477–497.

ASHURST, W. T. 1979 Numerical simulation of turbulent mixing layers via vortex dynamics. In *Turbulent Shear Flows* (ed. F. Durst, B. E. Launder, F. W. Schmidt & J. H. Whitelaw), vol. 1. p. 402. Springer.

ASHURST, W. T. & MEIRON, D. I. 1987 Numerical study of vortex reconnection. *Phys. Rev. Lett.* **58**, 1632.

BATCHELOR, G. K. 1967 *An Introduction to Fluid Mechanics.* Cambridge University Press.

BEALE, J. T. 1986 A convergent 3-D vortex method with grid-free stretching. *Math. Comp.* **46**, 401–424.

BERNAL, L. P. 1981 The coherent structure of turbulent mixing layers. Part 1. Similarity of the primary vortex structure. Part 2. Secondary streamwise vortex structure. Ph.D. thesis, Graduate Aeronautical Laboratories, California Institute of Technology.

BREIDENTHAL, R. 1981 Structure in turbulent mixing layers and wakes using a chemical reaction. *J. Fluid Mech.* **109**, 1–24.

BROWN, G. L. & ROSHKO, A. 1974 On density effects and large structure in turbulent mixing layers. *J. Fluid Mech.* **64**, 775–816.

CORCOS, G. M. & LIN, S. J. 1984 The mixing layer: deterministic models of a turbulent flow. Part 2. The origin of the three-dimensional motion. *J. Fluid Mech.* **139**, 67–95.

GREENGARD, C. 1986 Convergence of the vortex filament method. *Math. Comp.* **47**, 387–398.

JIMENEZ, J. 1983 A spanwise structure in the plane shear layer. *J. Fluid Mech.* **132**, 319–336.

JIMENEZ, J., COGOLLOS, M. & BERNAL, L. P. 1985 A perspective view of the plane mixing layer. *J. Fluid Mech.* **152**, 125–143.

KONRAD, J. H. 1976 An experimental investigation of mixing in two-dimensional turbulent shear flows with applications to diffusion-limited chemical reactions. Ph.D. thesis, Graduate Aeronautical Laboratories, California Institute of Technology.

LAMB, H. 1932 *Hydrodynamics.* Cambridge University Press.

LANG, D. 1985 Laser Doppler velocity and vorticity measurements in turbulent shear layers. Ph.D. thesis, Graduate Aeronautical Laboratories, California Institute of Technology.

LASHERAS, J. C., CHO, J. S. & MAXWORTHY, T. 1986 On the origin and evolution of streamwise vortical structures in a plane free shear-layer. *J. Fluid Mech.* **172**, 231–258.

LASHERAS, J. C. & CHOI, H. 1988 Three-dimensional instability of a plane, free shear layer: an experimental study of the formation and evolution of streamwise vortices. *J. Fluid Mech.* **189**, 53–86.

LEONARD, A. 1980 Vortex methods for flow simulation. *J. Comp. Phys.* **37**, 289–335.

LEONARD, A. 1985 Computing three-dimensional incompressible flows with vortex elements. *Ann. Rev. Fluid Mech.* **17**, 523–559.

LIN, S. J. & CORCOS, G. M. 1984 The mixing layer: deterministic models of a turbulent flow. Part 3. The effect of plane strain on the dynamics of streamwise vortices. *J. Fluid Mech.* **141**, 139–178.

MEIBURG, E. & LASHERAS, J. C. 1986 Comparison between experiments and numerical simulations of three-dimensional plane wakes. *Phys. Fluids* **30**, 623–625.

NAKAMURA, Y., LEONARD, A. & SPALART, P. 1982 Vortex simulation of an inviscid shear layer. *AIAA paper* 82-0948.

NEU, J. C. 1984 The dynamics of stretched vortices. *J. Fluid Mech.* **143**, 253–276.

PIERREHUMBERT, R. T. 1986 Remarks on a paper by Aref and Flinchem. *J. Fluid Mech.* **163**, 21–26.

PIERREHUMBERT, R. T. & WIDNALL, S. E. 1982 The two- and three-dimensional instabilities of a spatially periodic shear layer. *J. Fluid Mech.* **114**, 59–82.

RILEY, J. J., METCALFE, R. W. & ORSZAG, S. A. 1986 Direct numerical simulations of chemically reacting turbulent mixing layers. *Phys. Fluids* **29**, 406–422.

ROBINSON, A. C. & SAFFMAN, P. G. 1984 Three-dimensional instability of an elliptical vortex in a straining field. *J. Fluid Mech.* **142**, 451–466.

ROGERS, R. M. & MOIN, P. 1987 The structure of the vorticity field in homogeneous turbulent flows. *J. Fluid Mech.* **176**, 33–66.

SIGGIA, E. D. 1985 Collapse and amplification of a vortex filament. *Phys. Fluids* **28**, 794–805.

TSAI, C. Y. & WIDNALL, S. E. 1976 The stability of short waves on a straight vortex filament in a weak externally imposed strain field. *J. Fluid Mech.* **73**, 721–733.

WILLIAMSON, J. H. 1980 Low-storage Runge-Kutta schemes. *J. Comp. Phys.* **35**, 48–56.

ZABUSKY, N. J. 1981 Computational synergetics and mathematical innovation. *J. Comp. Phys.* **43**, 195–249.